Three-dimensional multimodal imaging and analysis of biphasic microstructure in a Ti–Ni–Sn thermoelectric material

Jason E. Douglas' , McLean P. Echlin, William C. Lenthe, Ram Seshadri, and Tresa M. Pollock

Citation: APL Materials **3**, 096107 (2015); doi: 10.1063/1.4931764
View online: http://dx.doi.org/10.1063/1.4931764
View Table of Contents: http://aip.scitation.org/toc/apm/3/9
Published by the American Institute of Physics

Three-dimensional multimodal imaging and analysis of biphasic microstructure in a Ti–Ni–Sn thermoelectric material

Jason E. Douglas,[1,2,a] McLean P. Echlin,[1] William C. Lenthe,[1] Ram Seshadri,[1,2,3] and Tresa M. Pollock[1,2]
[1]*Materials Department, University of California, Santa Barbara, California 93106, USA*
[2]*Materials Research Laboratory, University of California, Santa Barbara, California 93106, USA*
[3]*Department of Chemistry and Biochemistry, University of California, Santa Barbara, California 93106, USA*

(Received 28 May 2015; accepted 14 September 2015; published online 28 September 2015)

The three-dimensional microstructure of levitation melted $TiNi_{1.20}Sn$ has been characterized using the TriBeam system, a scanning electron microscope equipped with a femtosecond laser for rapid serial sectioning, to map the character of interfaces. By incorporating both chemical data (energy dispersive x-ray spectroscopy) and crystallographic data (electron backscatter diffraction), the grain structure and phase morphology were analyzed in a 155 μm × 178 μm × 210 μm volume and were seen to be decoupled. The predominant phases present in the material, half-Heusler TiNiSn, and full-Heusler $TiNi_2Sn$ have a percolated structure. The distribution of coherent interfaces and high-angle interfaces has been measured quantitatively. [http://dx.doi.org/10.1063/1.4931764]

Among the possible avenues for increasing the efficiency of global energy usage, thermoelectrics are an exciting, solid-state option. Thermoelectric materials, which convert an internal temperature gradient into a voltage and vice versa, have found applications in refrigeration as well as power generation from waste heat.[1–4] Semiconductors that form in the half-Heusler (hH) crystal structure are of particular interest[5,6] due to the very favorable electronic transport properties—conductivity and Seebeck coefficient—at relevant temperature regimes (between 500 °C and 800 °C), and because the common starting elements are relatively abundant and inexpensive. However, the efficiency of these materials suffers due to their relatively high thermal conductivities, typically >5 $Wm^{-1}K^{-1}$.[5] By contrast, the best performing thermoelectrics have thermal conductivities approaching 1 $Wm^{-1}K^{-1}$ or less.[7,8] The most common approaches to reduce the thermal conductivity of *n*-type, TiNiSn-based half-Heusler materials are grain size reduction, through extended ball-milling followed by rapid densification,[5] and isoelectronic substitution on the Ti atomic site, forming $Ti_{1-x-y}Zr_xHf_yNiSn$ alloys in which mass fluctuation at point defects[9,10] and strain in the lattice[5,11] act to scatter high-energy phonons.

A third approach that has been explored more recently in the literature is to introduce full-Heusler (fH) particles, of the composition XNi_2Sn (X = Ti, Zr, or Hf), into the matrix.[5,6,12–14] By preparing materials of the formula $XNi_{1+x}Sn$—where typically $x \leq 0.15$—intentionally biphasic materials have been engineered in which thermal conductivity is reduced by interfacial boundary scattering and strain effects. In addition, the presence of interstitial Ni defects in the half-Heusler structure is understood to play a role in phonon scattering,[15–17] and the electronic properties are potentially improved by hot-carrier filtering at the phase interface.[18]

[a]Electronic mail: jedouglas@mrl.ucsb.edu

These half-/full-Heusler composite materials $X\mathrm{Ni}_{1+x}\mathrm{Sn}$ share a commonality with the best-performing $\mathrm{Ti}_{1-x-y}\mathrm{Zr}_x\mathrm{Hf}_y\mathrm{NiSn}$ alloys, in that phase separation is seen to play a central role in the efficiency of the latter[19] in addition to the mass contrast effects. While $\mathrm{Zr}_z\mathrm{Hf}_{1-z}\mathrm{NiSn}$ materials tend to be single-phase with full solubility between the Zr and Hf, if $x + y < 1$ in $\mathrm{Ti}_{1-x-y}\mathrm{Zr}_x\mathrm{Hf}_y\mathrm{NiSn}$ the materials will separate into a Ti-rich half-Heusler phase and a Zr/Hf-rich half-Heusler phase.[20–22] This holds true in *p*-type $\mathrm{Ti}_{1-x-y}\mathrm{Zr}_x\mathrm{Hf}_y\mathrm{CoSb}$ as well.[23] Given the importance of phase separation in the most advanced half-Heusler based thermoelectrics, it is critical to understand the microstructure in order to relate composition to properties, as recognized in previous studies.

A challenging aspect of examining and quantifying microstructure in bulk materials is that while phases and grains are generally 3-D in nature, most microscopy techniques only allow for 2-D characterization, a planar micrograph of an exposed surface. This is further complicated by the fact that multiple types of data are often required to address a single microstructural question. Previous studies have explored two-phase alloys, such as the γ/γ' microstructure of Ni-base superalloys, by sequential imaging and focused-ion beam milling,[24] but the collection time is prohibitive for large volumes. And while some microstructural properties can be calculated from stereological analysis in 2-D, others such as permeability[25] and percolation are difficult or impossible to determine without 3-D tomography. X-ray tomography is commonly employed to acquire 3-D data, to study questions such as precipitate curvature upon solidification,[26] with the advantage of being able to collect large volumes quickly and non-destructively. However, the similar lattice parameters and poor absorption contrast between the phases precludes this approach for full-Heusler/half-Heusler mixtures.

When the excess Ni concentration x in $\mathrm{TiNi}_{1+x}\mathrm{Sn}$ exceeds 0.15 in induction-melted materials, we have previously measured an abrupt jump in the thermal conductivity, attributed to percolation of the metallic $\mathrm{TiNi}_2\mathrm{Sn}$ at the composition $\mathrm{TiNi}_{1.20}\mathrm{Sn}$.[14] In this letter, we detail a 3-D microstructural study of melt-prepared $\mathrm{TiNi}_{1.20}\mathrm{Sn}$ by use of the TriBeam tomography system,[27] a scanning electron microscope (SEM) equipped with a femtosecond laser (150 fs pulse) for serial sectioning. Femtosecond lasers have been demonstrated to achieve *in situ* material removal rates that are 5–6 orders of magnitude faster than conventional Ga^+ source focused ion beams (FIBs) while maintaining low-damage ablation surfaces[27] that can be directly probed with SEM microanalytical techniques such as energy dispersive x-ray spectroscopy (EDS) and electron backscatter diffraction (EBSD), for chemical and structural information respectively. We have collected a tomographic dataset, 155 μm × 178 μm × 210 μm in size, and used these data to study grain structure and phase morphology. In particular, we examine connectivity of the $\mathrm{TiNi}_2\mathrm{Sn}$ phase and the presence of high angle versus coherent interfaces between the phases, and relate these to the thermal transport properties of the bulk sample.

The material used for this study was prepared by levitation induction melting the respective constituent elements (Ti, Ni, and Sn in a ratio of 1:1.2:1) followed by a homogenizing heat treatment, described in detail in Ref. 14. A rectangular specimen just over 200 μm thick and 1 cm^2 in area was prepared for the TriBeam from this heat-treated material using a low speed cut-off saw with a diamond wafering blade. Along one edge, square pillars approximately 200 μm wide were cut to limit redeposition of ablating material onto the specimen. The dataset was collected from one of these pillars.

Femtosecond laser pulses with 780 nm wavelength and 1 kHz repetition rate were used to ablate material from the sample surface. The laser beam was scanned horizontally and parallel to the sample surface, ablating material with the low-fluence radial edge of Gaussian profile pulses.[27] Therefore, high resolution encoded piezoelectric stages control the slice thickness by incrementally raising the sample surface into the beam. As such, slices as thin as 100 nm may be removed. However, 2 μm slices were made for the $\mathrm{TiNi}_{1.20}\mathrm{Sn}$ samples due to the size of the dendritic microstructural features and the interaction volume of 20 keV EDS imaging (1 μm deep). In total, 89 slices were collected with EBSD and EDS maps at 0.7 μm step size, giving an overall voxel size of 0.7 μm × 0.7 μm × 2.0 μm. The total dataset collection required roughly 48 h for fully automated acquisition of all signals.

The procedure for reconstructing the dataset into a 3-D volume is outlined in Figure 1. All collected data are stored in an archival HDF5, binary, or Matlab file, with the ability to query any modality of information for any voxel. Phases were defined per slice using the expectation-maximization/maximization of the posterior marginals (EM/MPM) algorithm,[28] as implemented in BlueQuartz software EM/MPM Workbench, to threshold maps of the Ni EDS signal into three classes: hH TiNiSn, fH

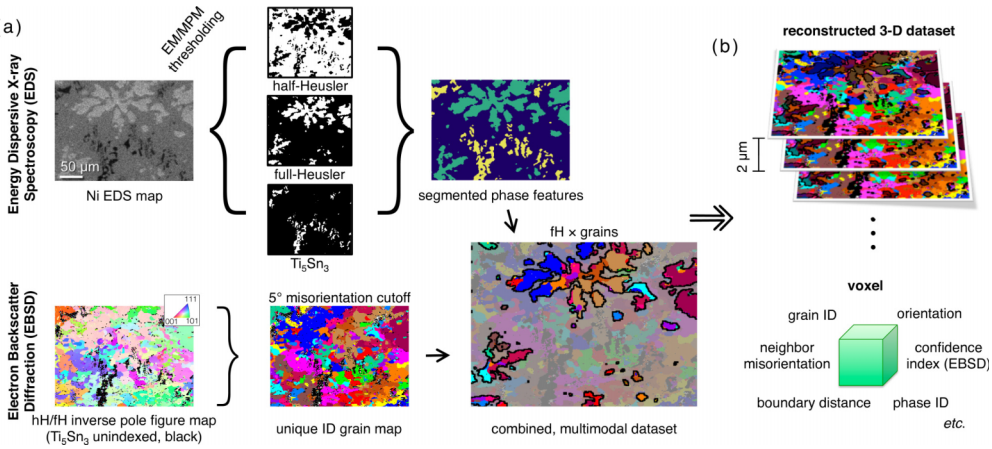

FIG. 1. Schematic process for data segmentation and reconstruction—decomposed to example 2-D maps for ease of view, though in practice all raw data are stored and retained at each voxel, and segmentation and analysis are performed in 3-D. (a) At each slice, chemical and crystallographic data are collected simultaneously and used, respectively, to segment phases and define unique grains. (b) These data reconstructed into a 3-D volume.

$TiNi_2Sn$, and a Ti–Sn binary phase, $Ti_5Ni_{1-y}Sn_3$, the three phases observed in the material by x-ray diffraction (XRD) and by EDS (considering Ti and Sn signal in addition to Ni).

EBSD data collected simultaneously were indexed to either fH or $Ti_5Ni_{1-y}Sn_3$ to gain orientation data; while EBSD can give higher resolution phase identification than EDS, which has an interaction volume of between 1 and 2 μm, the diffraction patterns given by hH and fH are too similar to be distinguishable by EBSD analysis software. The data of these two modalities, segmented EDS and EBSD orientation data, were then combined using the Dream3D software package,[29] in which volume reconstruction, stack alignment, data cleanup, property measurement, and data analysis were performed.

The complete reconstructed volume is shown in Figure 2(a), colored by phase. 20% of the voxels in the dataset are indexed as fH, a volume fraction that agrees well with that expected from the nominal composition as well as the mole fraction determined from synchrotron XRD analysis, 17%.[14] The coarse step size is not optimal for resolving the Ti–Sn binary phase, given the large aspect ratio and thinness of these features. However, the general morphology of each phase as indexed from the Ni EDS signal corresponds well with what we observe in backscatter electron and optical microscopy.

From this dataset, we isolate the largest contiguous fH features, the three largest of which are presented in Figure 2(b). The two largest features encompass 90% of fH volume fraction in the dataset, 55% and 35% individually. It is possible that the two features are connected through pathways that extend outside the collected dataset volume, especially since their boundaries within the dataset are separated by only 5 μm at points. The large spatial extent of fH connectivity—hundreds of microns in 3-D—suggests that the metallic fH phase has reached a percolation threshold in this sample, which could explain its notably higher thermal conductivity as compared to samples with less Ni.[14]

The multiple imaging modalities (EDS and EBSD), collected at every voxel, were leveraged to identify not only phase information but also the spatial location of grains and grain boundaries within the $TiNi_2Sn$ phase. Specifically, we can address whether or not these fH features are a single grain, which would result in high thermal conductivity due to the lack of boundaries where phonon scattering might occur. As seen in Figure 3, however, this is not the case. While the second largest fH feature (lower volume) is mostly of a single orientation within 10° of the average, the larger feature has a wide variability in internal misorientation up to 62.8°. This feature is comprised mainly of six different orientation clusters with several smaller grains dispersed throughout. This indicates that a region being monophasic does not necessarily correspond to it being a single orientation (i.e., a single grain) or, conversely, that grain boundaries do not necessarily indicate a phase boundary.

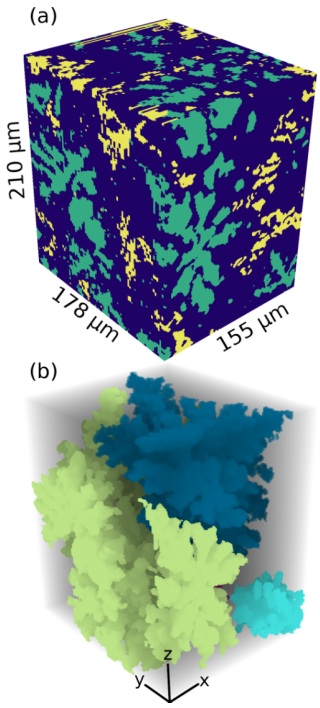

FIG. 2. Visualization of the $TiNi_{1.20}Sn$ dataset, 155 μm × 178 μm × 210 μm in size. (a) Surfaces of the volume colored by phase, where blue is TiNiSn, green is $TiNi_2Sn$, and yellow is a Ti–Sn binary. (b) Reconstructions of the three largest full-Heusler ($TiNi_2Sn$) phase regions of continuous connectivity, as shown with unique coloring.

As an alternative to partitioning the dataset by phase, it is also insightful to analyze the volume based on only crystallographic orientation. Phase boundaries are often defined *prima facie* as grain boundaries when analyzing EBSD data, but this is not appropriate for the hH/fH system. The two phases have very similar crystal structures, both cubic with a 3% lattice mismatch, and are

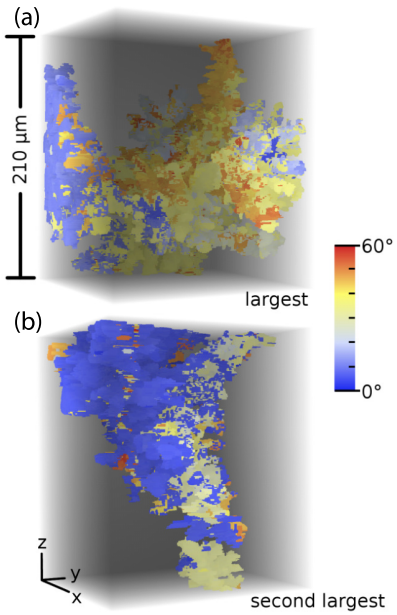

FIG. 3. The largest and second largest contiguous fH features, as partitioned from the volume by thresholding Ni EDS data. Each voxel is colored by its degree of misorientation from the average orientation of the feature. These and all subsequent images are shown from the same viewpoint.

known to form (semi)coherent interfaces.[13,14] As such, grains were analyzed with boundary locations defined only as interfaces with high crystallographic misorientation—here we use a voxel-to-voxel misorientation threshold of 5° and a minimum size cutoff of 25 voxels. By this measure, there are 2182 grains in the volume, as compared to the (chemistry-identified) 133 unique fH features >25 voxels in size and an almost completely connected hH phase. (99.992% of the latter phase belongs to a single feature, one of only 6 hH features >25 voxels.)

The resulting 11 grains with size greater than 100 000 μm^3 are reconstructed in Figure 4, constituting 92% of the cubic material volume (hH or fH) in the dataset. The largest grain is approximately 30% of the volume. Despite the large size of this grain, which has an equivalent diameter of 70 μm within the collected volume, the crystallographic orientation is extremely homogeneous throughout. As displayed in Figure 5(a), almost every part of the grain is oriented within 10° of the grain average. The few pockets of high internal misorientation (>15°, 21.1° at maximum) are less than 10 μm in diameter.

The voxels of the largest grain that are indexed as $TiNi_2Sn$ are presented in Figure 5(b). Approximately 30% of the grain volume is fH, the bulk of which is a part of the fH feature from Fig. 3(b). The fH phase in the interior of this grain indicates that a single orientation in these materials does not necessarily denote a single phase, and that phase boundaries can occur within a single grain. This is particularly striking because it demonstrates a high areal density of coherent hH/fH phase boundaries present throughout the material. The coherent interface persists for lengths greater than a hundred microns and acts to increase the boundary density within the material; the ratio of boundary-area to volume for this grain is 60% greater when both phase and grain boundaries are included, rather than just the latter. Given that grain and phase sizes within the volume are larger than typical phonon mean free path lengths when considered separately, these coherent interfaces will be important for scattering and thermal conductivity reduction. The coherency of fH with the hH is of additional significance as coherent boundaries, which account for just over half of the total

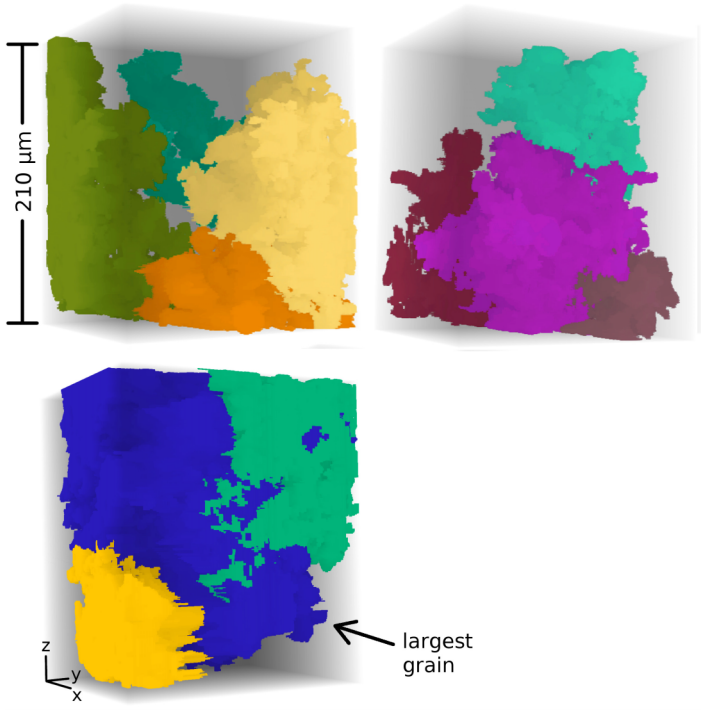

FIG. 4. The eleven largest grains of cubic material (hH and fH) within the volume, in which boundaries are defined only by a 5° voxel-to-voxel misorientation threshold on the EBSD data (i.e., no phase information). Colored only to distinguish for the eye and presented in three frames to ease visualization of all grains. The blue grain in the bottom frame is the single largest, making up ~30% of the volume.

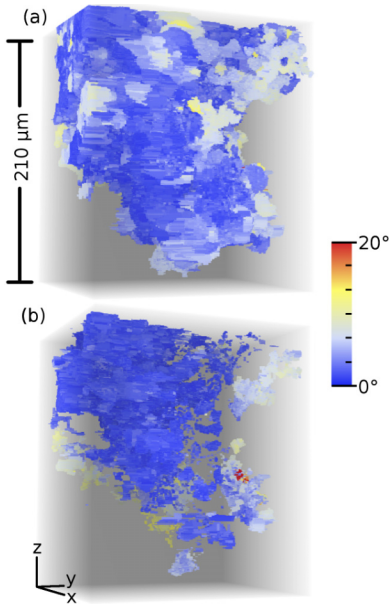

FIG. 5. (a) The single largest grain in the volume. (b) The same grain, but displaying only the voxels indexed as fH, which constitutes ~30% of the grain. Each voxel is colored by its degree of misorientation from the average orientation of the grain.

hH/fH interface area in the volume, are believed to damp phonon transport more strongly, due to the elastic strain fields and dislocations introduced into the material.[30]

In the grain of Figure 5, the shape and location of the fH are also noteworthy in that the fH appears to form the core of the grain. Due to the higher melting temperature of $TiNi_2Sn$ as compared to TiNiSn, we have posited that the fH solidifies first in $TiNi_{1+x}Sn$ materials prepared by the induction melting process, as evidenced by the dendritic morphology of the features.[14] This is supported by the grain structure observed here: fH particles solidify first in the melt, onto which heterogeneous hH nucleation occurs, eventually growing to the observed grain structure. The areal density of grain boundaries is 47% greater within the hH ($0.33\,\mu m^{-1}$) than the fH ($0.23\,\mu m^{-1}$), likely because nucleation of isolated fH dendrites initially occurs and subsequently the crystals impinge—and grain boundaries form—more frequently in the interdendritic hH regions. With the similarity of the two crystal structures, this sequence would also predict the observed large high areas of coherent interfaces.

The misorientation distribution function (MDF), Figure 6, shows that the grain boundary character is effectively independent of the structure. Here, boundary is defined as voxel faces that are bounded by voxels belonging to two different grains segmented in the volume. Intraphase and interphase boundaries show the same distribution, and there is almost an equal area of coherent and incoherent interface between TiNiSn and $TiNi_2Sn$. This suggests that the MDF is strongly influenced by the solidification path and orientation relationship between the fH and hH. Because of these factors, neither EBSD nor EDS can be used to determine the boundaries of this system independently. The MDF deviates from a uniformly random cubic distribution,[31] exhibiting more low-angle boundaries (<15°) and a peak near 30°. The peak likely corresponds to a coincident site lattice (CSL) boundary, however current algorithms for calculating boundary misorientation in 3-D datasets do not support boundary character determination based on local misorientation.

While the dataset collection volume was initially chosen to capture the scale of phase features in 2-D SEM micrographs, 100 μm or smaller, we see in 3-D that these grains and features can approach or exceed the edge lengths of our collected volume. As such, in the future a larger dataset may be required to accurately characterize some quantities such as maximum grain size. However, a large number of unique grains and phase features are able to be captured, which also appears to be a representative volume for a number of other microstructural features such as connectivity, phase boundary *versus* grain boundary location, and the relative abundance of boundary

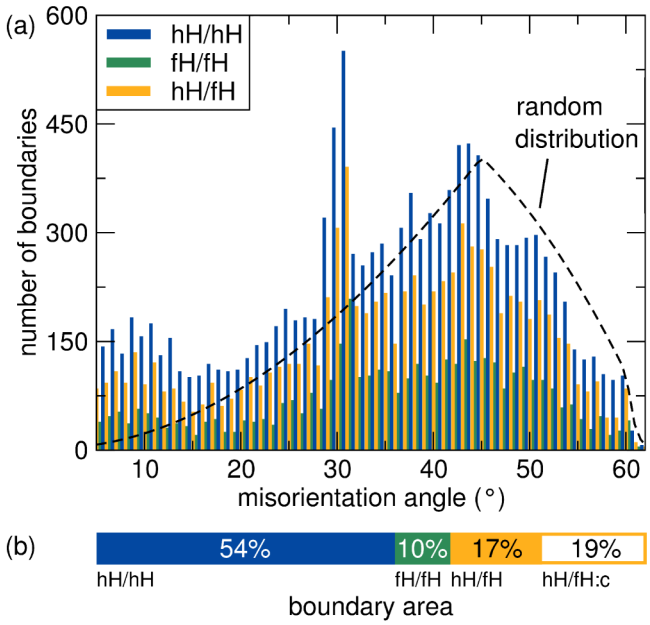

FIG. 6. (a) Misorientation distribution function for grain boundaries (GB) at each of three interfaces in the volume: TiNiSn/TiNiSn (hH/hH), TiNiSn/$TiNi_2Sn$ (hH/fH), and $TiNi_2Sn$/$TiNi_2Sn$ (fH/fH). The three are nearly identical. Dashed line is the Mackenzie distribution for randomly oriented grains in a cubic material.[31] (b) Relative fraction of the total GB area comprised of each interface, as well as coherent hH/fH interface (hH/fH:c).

types. Simultaneously, this study has helped develop reconstruction and analysis techniques for 3-D microstructural data.

In summary, we have used the new TriBeam tomography instrument to study phase and grain morphology in $TiNi_{1.20}Sn$ prepared by induction melting. With this technique, we were able to study a large, three-dimensional dataset that incorporates both chemical (EDS) and crystallographic (EBSD) data. We find that the fH phase appears to be percolated in this sample, with almost all of the fH phase contained in one of two contiguous features. Half- and full-Heusler coherency are maintained over large interfacial areas. In this material, we observe that phase boundaries do not necessarily coincide with grain boundaries and vice versa. The fact that phase boundaries and grain boundaries are decoupled means there is a higher density of interfaces than would be present otherwise, potentially increasing phonon scattering within the material. While the effect of percolated metallic pathways dominated interfacial scattering in this sample, the separably controllable grain boundary character and fH phase distribution present an opportunity for the optimization of microstructure in biphasic hH-based thermoelectric materials.

This work was supported by the MRSEC Program of the National Science Foundation through DMR-1121053. J.E.D. is supported by the National Science Foundation Graduate Research Fellowship Program under Grant No. 1144085. TriBeam development and W.C.L. are supported by the Air Force Research Laboratory Center of Excellence (Grant No. FA9550-12-1-0445). We would also like to thank Stuart Wright (EDAX) for OIM Analysis software support. The Materials Research Laboratory is a member of the NSF-supported Materials Research Facilities Network.

[1] J. R. Sootsman, D. Y. Chung, and M. G. Kanatzidis, Angew. Chem., Int. Ed. **48**, 8616 (2009).
[2] K. Smith and M. Thornton, *Feasibility of Thermoelectrics for Waste Heat Recovery in Conventional Vehicles* (NREL, U.S. Department of Energy, 2009).
[3] T. M. Tritt, Annu. Rev. Mater. Res. **41**, 433 (2011).
[4] M. Zebarjadi, K. Esfarjani, M. S. Dresselhaus, Z. F. Ren, and G. Chen, Energy Environ. Sci. **5**, 5147 (2012).
[5] S. Chen and Z. Ren, Mater. Today **16**, 387 (2013).
[6] J.-W. G. Bos and R. A. Downie, J. Phys.: Condens. Matter **26**, 433201 (2014).
[7] M. W. Gaultois and T. D. Sparks, Appl. Phys. Lett. **104**, 113906 (2014).
[8] L. D. Zhao, S. H. Lo, Y. Zhang, H. Sun, G. Tan, C. Uher, C. Wolverton, V. P. Dravid, and M. G. Kanatzidis, Nature **508**, 373 (2014).

[9] A. Peterson, S. Bhattacharya, T. M. Tritt, and S. J. Poon, J. Appl. Phys. **117**, 035706 (2015).
[10] H. Xie, H. Wang, Y. Pei, C. Fu, X. Liu, G. J. Snyder, X. Zhao, and Y. Zhu, Adv. Funct. Mater. **23**, 5123 (2013).
[11] J. Schmitt, Z. M. Gibbs, G. J. Snyder, and C. Felser, Mater. Horiz. **2**, 68 (2015).
[12] H. Hazama, M. Matsubara, R. Asahi, and T. Takeuchi, J. Appl. Phys. **110**, 063710 (2011).
[13] Y. W. Chai and Y. Kimura, Acta Mater. **61**(18), 6684 (2013).
[14] J. E. Douglas, C. S. Birkel, N. Verma, V. M. Miller, M.-S. Miao, G. D. Stucky, T. M. Pollock, and R. Seshadri, J. Appl. Phys. **115**, 043720 (2014).
[15] C. Colinet, P. Jund, and J.-C. Tédenac, Intermetallics **46**, 103 (2014).
[16] J. E. Douglas, P. A. Chater, C. M. Brown, T. M. Pollock, and R. Seshadri, J. Appl. Phys. **116**, 163514 (2014).
[17] D. T. Do, S. D. Mahanti, and J. J. Pulikkoti, J. Phys.: Condens. Matter **26**, 275501 (2014).
[18] Y. Liu, P. Sahoo, J. P. A. Makongo, X. Zhou, S.-J. Kim, H. Chi, C. Uher, X. Pan, and P. F. P. Poudeu, J. Am. Chem. Soc. **135**, 7486 (2013).
[19] M. Schwall and B. Balke, Phys. Chem. Chem. Phys. **15**, 1868 (2013).
[20] J. Krez, J. Schmitt, G. J. Snyder, C. Felser, W. Hermes, and M. Schwind, J. Mater. Chem. A **2**, 13513 (2014).
[21] R. A. Downie, D. A. MacLaren, and J.-W. G. Bos, J. Mater. Chem. A **2**, 6107 (2014).
[22] K. Gałazka, S. Populoh, L. Sagarna, L. Karvonen, W. Xie, A. Beni, P. Schmutz, J. Hulliger, and A. Weidenkaff, Phys. Status Solidi A **6**, 1259 (2014).
[23] E. Rausch, B. Balke, S. Ouardi, and C. Felser, Phys. Chem. Chem. Phys. **16**, 25258 (2014).
[24] M. D. Uchic, M. DeGraef, R. Wheeler, and D. M. Dimiduk, Ultramicroscopy **109**, 1229 (2009).
[25] M. P. Echlin, A. Mottura, M. Wang, P. J. Mignone, D. P. Riley, G. V. Franks, and T. M. Pollock, Acta Mater. **64**, 307 (2014).
[26] J. W. Gibbs and P. W. Voorhees, Integr. Mater. Manuf. Innovation **3**, 6 (2014).
[27] M. P. Echlin, A. Mottura, C. J. Torbet, and T. M. Pollock, Rev. Sci. Instrum. **83**, 023701 (2012).
[28] J. P. Simmons, P. Chuang, M. Comer, J. E. Spowart, M. D. Uchic, and M. De Graef, Modell. Simul. Mater. Sci. Eng. **17**, 025002 (2009).
[29] M. A. Groeber and M. A. Jackson, Integr. Mater. Manuf. Innovation **3**, 1 (2014).
[30] J. He, J. R. Sootsman, S. N. Girard, J.-C. Zheng, J. Wen, Y. Zhu, M. G. Kanatzidis, and V. P. Dravid, J. Am. Chem. Soc. **132**, 8669 (2010).
[31] J. K. Mackenzie, Biometrika **45**, 229 (1958).